Theor Chem Acc (2011) 128:757–767
DOI 10.1007/s00214-010-0790-y

REGULAR ARTICLE

A 3D-analysis of the Cl^-–benzene dimer solvation by Ar atoms

F. Huarte-Larrañaga · A. Aguilar · J. M. Lucas · M. Albertí

Received: 28 June 2010 / Accepted: 31 July 2010 / Published online: 28 August 2010

Abstract The solvation of the Cl^-–benzene (Cl^-–Bz) aggregate by Ar atoms has been investigated employing molecular dynamics (MD) simulations. The gradual evolution from cluster rearrangement to solvation dynamics is discussed by considering ensembles of n (n = 1,...,30) Ar atoms around the Cl^-–Bz clusters. The energetic of the solvated cluster is decomposed as a sum of pairs (including both the Ar–Ar and the Cl^-–Ar terms), Cl^-–Bz and Ar–Bz interactions and their relative contributions are analyzed as a function of the cluster size. The geometrical distribution of Ar atoms around Cl^-–Bz is investigated in terms of radial distribution functions (RDF), bidimensional (2D) angular distributions and tridimensional (3D) probability densities. The variation on the spatial distribution of the Ar atoms around Cl^-–Bz when the Ar number increases is investigated from a novel prospective, employing spherical coordinates of the solvent atoms within an inertial reference frame. Isomerization processes are also studied.

Keywords Molecular dynamics · Solvation · Radial distribution function · π–anion interactions

1 Introduction

The importance of noncovalent intermolecular interactions is presently acknowledged in several research fields, such as Biochemistry or Material Science. These interactions control different phenomena as for instance, the formation of weak hydrogen [1, 2] bonds, molecular recognition and selection processes [3–5] or the competitive solvation of ions [2, 6, 7]. These phenomena are present in molecular aggregates involving organic molecules [2, 4–6, 8–16] and in particular in aromatic compounds, among which benzene (Bz) is one of the most representative examples. Benzene, due to its large permanent quadrupole moment [17, 18], is able to interact with both cations and anions giving rise to the so-called cation-π and anion-π interactions, respectively. The electrostatic contribution is very important in these interactions but they are also affected by dispersion energies which, to be accurately described by ab initio calculations, require the use of large basis sets to include properly the electron correlation [19]. Moreover, at short range, the exchange repulsion effects also play an important role, which in the aromatic compounds affect mainly the "on-plane" approaches of ions to the aromatic ring and, because of the high polarizability of the aromatic rings, the induction effects can be very important. This means that anion-π interactions are governed by the combination of various components of the noncovalent intermolecular interaction. Unfortunately, it is quite difficult to accurately characterize the relative role played by the various components of noncovalent intermolecular interactions because, in general, they are much weaker than those leading to the usual chemical bonds. In spite of these difficulties, the important role that anion-π interactions can play in several fields, as in the design of new receptors stereoselectively binding anionic guests [20, 21], in organic synthesis [22, 23], in solvation in heterogeneous media [24], as well as in anion recognition processes [25, 26], has inspired a revisitation of this topic [27–29] and there has been a renewed interest in the investigation into this kind of

Published as part of the special issue celebrating theoretical and computational chemistry in Spain.

F. Huarte-Larrañaga (✉) · A. Aguilar · J. M. Lucas · M. Albertí
IQTCUB, Departament de Química Física, Universitat de Barcelona, Barcelona, Spain
e-mail: fermin.huarte@ub.edu

interactions, emphasizing the possible role of anion-π interactions in molecular anion recognition [30]. In addition to this, most of the chemical and biochemical processes of interest take place in solution and therefore the introduction of a solvent in both the theoretical simulations and experiments can be important. However, in spite of the great effort invested in the experimental characterization of solvation, the microscopic details of solvation of ions still escape accurate experimental investigations. Molecular dynamics (MD) simulations can, in principle, fill the gap of the experimental limitations and thus provide an atomic perspective of the structure and dynamics of the solvation shell, which is regarded as a fundamental piece in view of the emerging field of nanobiotechnology. The experimental advances in generating van der Waals clusters fostered theoretical studies on their structure and dynamical behavior [31]. In particular, the study of van der Waals clusters formed by a solute molecule embedded in a flexible cage of solvent atoms (or molecules) has been recognized as a powerful tool to investigate the process of solvation [31, 32]. This is the case of aromatic molecule-rare gas complexes that can be viewed as a solute (aromatic) molecule in a well-characterized local solvent configuration (rare gas) [33, 34]. Rare gases in general, with their formally filled valence shell, can be considered as the simplest of solvents [31], and in particular, Ar atoms are popular surrogates of water for molecular dynamics simulations, mainly because of their similar polarizability.

Bearing in mind that, for large systems, ab initio methods are in general confined to the calculation of most stable geometries of individual molecules, it is obvious that the use of semiempirical methods is of fundamental importance, specially when the related potential energy surface (PES) needs to be assembled. In the recent past, some of the authors have developed a semiempirical potential model, constructed by decomposing the nonelectrostatic interaction in atom(ion)-bond contributions, expressed by means of an Improved Lennard Jones (ILJ) function [35, 36]. The model has been extended to investigate rare gas(Rg)–Bz aggregates [37–39]. By combining the nonelectrostatic contribution with the electrostatic one, the model was first applied to the study of alkali cation (M^+)–Bz and halogen anion (X^-)–Bz systems and tested by comparing the predicted results [40, 41] with ab initio calculations [42, 43]. The potential model was next employed to study solvation by means of Ar atoms in (M^+)–Bz cluster [44–47] and I^-–Bz aggregate [48] clusters. Also, the isomerization processes in small aggregates of Cl^-–Bz–Ar(n) (n = 1, 2, 3) [49] have been investigated.

In the present study, we are interested in investigating the gradual evolution from cluster rearrangement to solvation dynamics applied to the Cl^-–Bz system solvated by Ar atoms. In contraposition with the well-known cation-π interactions, the interactions between anions and benzene are referred here as anion-π interactions, in spite of the preferred in-plane configurations found when anions approach Êbenzene. With this purpose in mind, we have carried out extensive MD simulations of the Cl^-–Bz dimer including an increasing number of Ar atoms acting as a solvent. Bearing in mind the high number of Ar atoms considered and in view of the recently reported results of ab initio calculations [41, 43], the investigation has been made by using the semiempirical method based on ion-bond decomposition of the interaction. We have extracted energetic information from our calculations and analyzed the different components of the nonbonding interaction energies. Besides the energetic analysis, we have paid special attention to the spatial distribution of the solvation shell. In order to do this, we have transformed the raw outcome of our MD trajectories to an inertial reference frame, centered at the Bz center of mass (c.o.m.) and computed spherical coordinates of all surrounding Ar atoms. This strategy has allowed us to calculate monodimensional information such as radial distribution functions (RDF) but also two-dimensional (2D) and three-dimensional (3D) distributions have been performed, which highlight the importance of obtaining a full-dimensional picture of solvation. We have finally analyzed cluster isomerizations in terms of the spherical coordinates. The paper is structured as follows: in Sect. 2, the formulation of the particular potential energy function employed in this work is outlined and the procedure followed to obtain the three-dimensional picture of the solvation shell as well as the numerical details of the MD simulations is given in Sect. 3. In Sect. 4 the results are presented and discussed and, finally, Sect. 4 concludes.

2 The potential energy surface for Cl^-–Benzene–$Ar_{(n)}$ aggregates

The total potential energy function (V) is decomposed at first as sum of pair contributions, including the Ar–Ar and Ar–Cl^- terms and three-body contributions, including the Ar–Bz and the Cl^-–Bz ones. The Ar–Ar, Ar–Cl^- and Ar–Bz interactions are governed by forces of nonelectrostatic nature, while the Cl^-–Bz interaction accounts for both electrostatic and nonelectrostatic effects. V can then be evaluated as,

$$V = V_{\mathrm{Ar-Bz}} + V_{\mathrm{Cl^-Bz}} + V_{\mathrm{pair}} = V_{\mathrm{nel}} + V_{\mathrm{el}} \quad (1)$$

where V_{nel} and V_{el} represent the nonelectrostatic and electrostatic contributions respectively. $V_{\mathrm{Ar-Bz}}$ represents the interaction between n Ar atoms and Bz and it is decomposed as "n" independent interactions, each one expressed as a sum of 12 terms of the atom-bond type (6 Ar–CC and 6 Ar–CH),

$$V_{\mathrm{Ar-Bz}} = V_{\mathrm{atom-bond}} = \sum_{k=1}^{n}\left(\sum_{i=1}^{6} V_{(\mathrm{Ar})_k-(\mathrm{CC})_i} + \sum_{i=1}^{6} V_{(\mathrm{Ar})_k-(\mathrm{CH})_i}\right). \quad (2)$$

$V_{\mathrm{Cl^--Bz}}$ represents the interaction between Cl^- and Bz and is decomposed by nonelectrostatic and electrostatic contributions. The nonelectrostatic one, here represented by $V_{\mathrm{ion\text{-}bond}}$, is decomposed as a sum of 12 ion-bond contributions (6 Cl^-–CC and 6 Cl^-–CH),

$$V_{\mathrm{ion-bond}} = \sum_{i=1}^{6} V_{\mathrm{Cl^--(CC)_i}} + \sum_{i=1}^{6} V_{\mathrm{Cl^--(CH)_i}} \quad (3)$$

Accordingly, $V_{\mathrm{Cl^-Bz}}$ is given by,

$$V_{\mathrm{Cl^-Bz}} = \sum_{i=1}^{6} V_{\mathrm{Cl^--(CC)_i}} + \sum_{i=1}^{6} V_{\mathrm{Cl^--(CH)_i}} + V_{\mathrm{el}} \quad (4)$$

The electrostatic contribution, V_{el}, is calculated by means of Coulomb charge–charge interactions between the anion, with a charge of -1 a.u. placed on it and the charge distribution of Bz that has positive charges of 0.09246 a.u. placed on the H atoms and two negative charges of -0.04623 a.u. placed above and below of each C atom (with respect to the aromatic ring) separated by 1.905 Å. This charge distribution asymptotically corresponds to the ion–quadrupole interaction [50, 51]. Finally, V_{pair} is expressed as sum of all possible pair interactions,

$$V_{\mathrm{pair}} = \sum_{i=1}^{n} V_{\mathrm{Cl^--Ar}_i} + \sum_{i=1}^{n-1}\sum_{j>i}^{n} V_{\mathrm{Ar}_i-\mathrm{Ar}_j} \quad (5)$$

The individual contributions to the $V_{\mathrm{ion-bond}}$, $V_{\mathrm{atom-bond}}$ and V_{pair} interactions are described by means of Improved Lennard Jones functions (V_{ILJ}), which include an additional parameter in comparison with the LJ function. The same functional form (only with small differences in the variables) is used to describe both, the two-body (pair) and the three-body (atom-bond and ion-bond) terms given that, in the potential model, the interactions are described between dispersion centers rather than between atoms. In the pair interactions, the dispersion centers are placed on the atoms (or on the ion), while in the atom(ion)–bond interactions, one dispersion center is placed on the atom (or on the ion) and the other one on the center of the bond. Thus, when V_{ILJ} is used to calculate the pair interactions (Cl^-–Ar and Ar–Ar), it depends only on one variable, the interatomic distance represented by r (see the left-hand side of Fig. 1). Instead, when V_{ILJ} is used to calculate the atom(ion)–bond interactions (Ar–CC, Ar–CH, Cl^-–CC and Cl^-–CH), it depends on two variables, the distance between the ion and the center of the bond, r, and the angle, γ, that the **r** vector forms with the bond (see the right hand side of Fig. 1).

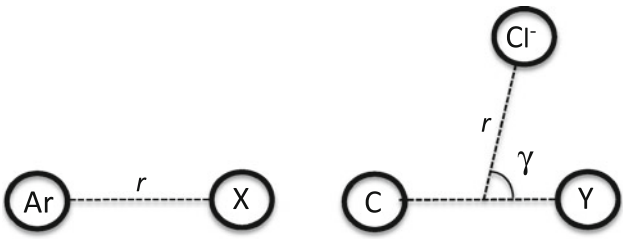

Fig. 1 *Left hand panel* Pair potential variables, X represents Ar and Cl^-. *Right hand panel* Ion-bond variables, Y represents C and H atoms

As it can be seen in the following equation,

$$V_{\mathrm{ILJ}} = \varepsilon\left[\frac{m}{n-m}\left(\frac{r_0}{r}\right)^n - \frac{n}{n-m}\left(\frac{r_0}{r}\right)^m\right] \quad (6)$$

the ILJ function looks very similar to the LJ one. However, in the ILJ function, the exponent of the repulsive part of the potential, n, is no longer a constant. The n exponent, which defines the falloff of the repulsion, is expressed as

$$n = \beta + 4.0\left(\frac{r}{r_0}\right)^2 \quad (7)$$

where β is the characteristic ILJ parameter, additional with respect to those of the LJ potential, which is related to the hardness of the interacting partners [35, 37] and can be adjusted according to the properties of the systems. In the effective potentials represented by Eq. 6, the first term (positive) represents the size-repulsion contribution and the second one (negative) represents dispersion plus induction effective attraction. The advantages of using ILJ instead of LJ have been discussed in other studies (see for instance [35]). In the ILJ formulation, the well depth and the equilibrium distance, ε and r_0, having a physical meaning, are considered to have a universal character. Accordingly, these parameters can be transferred from one system to another having the same pair or atom(ion)–bond contributions, even when the different systems are in different environments.

For pair interactions, the only difference between ILJ and LJ functions is in the definition of the n exponent. However, for atom(ion)–bond interactions, ε and r_0 depend on the γ angle and are calculated from two limit approaches of the atom (or ion) to the bond (perpendicular and parallel) [40, 44–47] for which the corresponding parameters ($\varepsilon_\perp$, $\varepsilon_\parallel$, $r_{0\perp}$ and $r_{0\parallel}$) are calculated using the polarizability of the atoms (or ions) and the effective perpendicular and parallel components of the bond polarizabilities [52]. These parameters are given in Table 1. Once these limiting parameters have been determined, ε and r_0 can be easily derived by applying simple trigonometric formula (see for instance [45]). The n parameter depends only on r for pair interactions, while it depends on both r and γ for the ion-bond and atom-bond ones. This is given by the angular dependence of r_0. The m parameter, the exponent

Table 1 Perpendicular and parallel components of the well depth ($\varepsilon_\perp$, $\varepsilon_\parallel$) and of the equilibrium distances ($r_{0\perp}$, $r_{0\parallel}$) for Cl^-–CC, Cl^-–CH, Ar–CC and Ar–CH interactions

ion-bond	$\varepsilon_\perp$/meV	$\varepsilon_\parallel$/meV	$r_{0\perp}$/Å	$r_{0\parallel}$/Å
Cl^-–CC	16.37	59.64	3.832	4.073
Cl^-–CH	25.48	28.60	3.655	3.839
Ar–CC	3.895	4.910	3.879	4.189
Ar–CH	4.814	3.981	3.641	3.851

Table 2 ε and r_0 parameters used to calculate Cl^-–Ar and Ar–Ar interactions

X–Ar	ε/ meV	r_0/Å
Cl^-–Ar	64.870	3.710
Ar–Ar	12.370	3.757

Table 3 β parameters used to describe Cl^-–CC, Cl^-–CH, Ar–CC, Ar–CH, Cl^-–Ar and Ar–Ar interactions

	Cl^-–CC	Cl^-–CH	Ar–CC	Ar–CH	Cl^-–Ar	Ar–Ar
β	7.0	7.0	9.0	9.0	7.8	9.0

of the attractive term in Eq. 6, is selected accordingly with the interaction: $m = 6$ for Ar–Ar, Ar–CC and Ar–CH interactions (neutral-neutral), while $m = 4$ for the Cl^-–Ar, Cl^-–CC and Cl^-–CH ones (ion-neutral).

All the involved pair interactions, $V_{Cl^- - Ar}$ and V_{Ar-Ar}, as indicated before, are also described by means of the ILJ function, and ε and r_0 parameters are given in Table 2. The corresponding β parameters are given in Table 3.

3 Simulation details

Dynamics simulations of the Cl^-–Bz–$Ar_{(n)}$ systems have been carried out using the DL_ POLY MD program [53]. The calculations have been performed by considering a microcanonical ensemble (NVE) of atoms and sweeping over increasing values of the total energy (E_{total}). This increase in E_{total} originates increases on both the averaged potential (E_{cfg}) and kinetic (E_{kin}) energies.

Within the NVE ensemble, E_{total} is conserved and the total energy is calculated at each step from the values of the kinetic and the potential energies. Geometries and energies are averaged over the MD trajectory to obtain the mean values associated with the simulation. A time step of 1 fs has been used in all the simulations presented here, integrating the MD trajectories up to final time of 14 ns. The time step chosen is large enough to keep the fluctuations of E_{total} well below 10^{-5} meV. Previous to the actual MD simulation, an initial equilibration period has been introduced running the trajectory for 0.1 ns (using the same time step) during which the velocities of all atoms are re-scaled to match the input temperature, every 10 integration steps. After this equilibration period, the system is considered to be thermalized and no further constrains are imposed. This equilibration period has been excluded from the statistical analysis at the end of the trajectory.

An initial configuration for each Cl^-–Bz–$Ar_{(n)}$ cluster has been generated by placing the Cl^-–Bz dimer close to its minimum energy configuration and then solvating it by randomly placing Ar atoms at distances between 4.0 and 9.0 Å. It is important to point out at this stage that the benzene molecule is kept rigid throughout all our simulations. We do not believe that Bz internal motion can change significantly the results presented here. From this configuration, an initial calculation is carried out at a temperature of 30 K with an equilibration period of 1 ns. The simulation at each new total energy is performed by starting a new trajectory from the final configuration, velocities and forces of the previous run (performed at a lower temperature) and re-scaling (0.1 ns) to the new temperature value. The size of the clusters investigated here ranges from aggregates containing one single Ar atom to a shell of 30 Ar atoms.

As already mentioned, results are obtained from each MD trajectory by extracting the time averages of energies and atom coordinates. To help in the rationalization of the results, E_{cfg} has been defined as the average of the total potential energy over all the accessible configurations at the chosen value of E_{total}. This potential energy has been decomposed in 3 contributions associated with the chloride–benzene ($E_{Cl^- - Bz}$), argon–benzene (E_{Ar-Bz}) and all pair interactions (E_{pair}).

Besides the energetic information, we have already discussed in the introduction section how MD simulations offer the possibility to analyze processes with molecular detail. In order to do this, we have extracted radial distribution functions (RDF) of the Ar solvent atoms with respect to the benzene molecule center of mass (c.o.m.) and also with respect to the Cl^- anion. This type of distribution function is nowadays routinely obtained from standard MD simulations. We find, however, that this information is often insufficient in multidimensional systems, specially where there is a strong anisotropy.

Thus, in order to get a deeper understanding of the structure of the solvated cluster, we have constructed the three-dimensional solvation shell from the outcome of the MD trajectories, employing spherical coordinates in an inertial reference frame. For each configuration sampled in the dynamics trajectory, excluding the equilibration, the positions of all atoms are transformed to the benzene

principal axes of inertia reference frame. Given the symmetry of the C_6H_6 hexagon, we need to introduce some additional requirements to make the transformation univocal throughout the analysis. This allows us to specify the relative position of Ar solvent and the Cl^- atoms with respect to the (now) fixed benzene molecule. We have found particularly useful to employ spherical coordinates in this context: r (in Å) as the distance of the atom to the Bz c.o.m., θ the orientation angle with respect to the vector normal to the benzene plane, and ϕ the azimuthal angle.

The RDFs are then calculated by integrating

$$RDF(r) = \int_0^{\pi} \sin\theta \mathrm{d}\theta \int_0^{2\pi} \mathrm{d}\phi\, r^2 \rho(r,\theta,\phi), \tag{8}$$

where $\rho(r, \theta, \phi)$ is the probability density. In the case of Ar, $\rho(r, \theta, \phi)$ is obtained averaging over all time steps and all argon atoms. Similarly, we can integrate over the radial coordinate to obtain angular distributions.

$$d(\theta,\phi)) = \int_{r1}^{r2} \mathrm{d}r \rho(r,\theta,\phi), \tag{9}$$

This procedure has allowed us to obtain the usual RDFs and, in addition to this, represent the angular distribution corresponding to the different maxima in the RDF. This yields a tridimensional picture of the solvation shell. Finally, we have completed our geometrical analysis of the solvation in the Cl^-–Bz–$Ar_{(n)}$ system by representing, in the inertial reference frame, 3D probability density isosurfaces. To obtain and visualize these isosurfaces, the "Volmap" tool from the VMD package [54] has been employed.

4 Results

We have studied a wide range of cluster sizes employing the previously mentioned tools, starting with the Cl^-–Bz–Ar aggregate, with one single argon atom, up to the largest cluster calculated, containing 30 argon atoms. All the calculations have been run at low values of E_{total}, leading to small increases in E_{kin} (temperature values close to 30 K). The averaged configuration energies and their different components are listed in Table 4. In order to give an indication of the total energy available in the system, the actual averaged temperature of the simulation is given in the second column of the table. As expected, the configuration energy increases as the system grows in size. Thus, the inclusion of more Ar atoms in the model allows the system to be more stable. An interesting feature is revealed if we consider the separate components of E_{cfg} and their relative contributions. For the very small clusters, with

Table 4 Cl^-–Bz–$Ar_{(n)}$ configuration energy (E_{cfg}) and its components as a function of the cluster size

n	T	E_{cfg}	$E_{Cl^- -Bz}$	$E_{Ar\text{-}Bz}$	E_{pairs}
1	26.6	−402.2	−311.2	−27.5	−63.5
2	38.1	−487.7	−309.2	−45.9	−132.7
3	23.6	−588.7	−311.2	−67.0	−210.4
4	39.8	−672.7	−308.8	−79.6	−284.4
5	38.4	−768.6	−309.0	−92.6	−367.0
6	36.6	−863.8	−309.2	−99.8	−454.7
7	33.5	−965.9	−309.7	−104.78	−551.4
8	25.7	−1,081.9	−310.9	−107.1	−664.0
9	34.8	−1,167.2	−309.6	−108.0	−749.6
12	36.1	−1,481.2	−309.5	−198.8	−1,027.0
15	37.3	−1,706.3	−309.9	−218.1	−1,178.3
18	31.7	−1,923.7	−317.1	−274.7	−1,331.9
22	31.7	−2,190.7	−317.1	−277.6	−1,597.7
25	29.9	−2,402.8	−317.2	−313.9	−1,776.0
30	33.6	−2,718.5	−316.7	−297.0	−2,104.8

Temperature values are in Kelvin and energies in meV

n smaller than 4, the stability of the system is mainly due to the chloride–benzene interaction. Indeed, $E_{Cl^- -Bz}$ represents a 77% of the total potential energy of the aggregate with one single solvent atom. This same interaction represents less than 25% of the total potential energy in Cl^-–$Bz–Ar_{12}$ and is only slightly above 10% when $n = 30$. This effect is, however, not given by a decrease in the absolute interaction energy between Cl^- and Bz but rather the appearance of increasing Ar–Bz, Ar–Cl^- and Ar–Ar interactions. The two latter interactions, collected in E_{pairs}, clearly dominate the potential energy for Cl^-–$Bz–Ar_n$ clusters larger than $n = 6$. The addition of each additional Ar atom to the cluster accounts for an increase of approximately −74 meV in E_{pairs}. This correlation is not shown by $E_{Ar–Bz}$, in spite of its increase, manifesting the preference of Ar atoms to solvate chloride, at least for the cluster sizes investigated here. It is evident, however, from the trends shown in the table that the emerging interactions do not shield the interaction between the halogen anion and the aromatic molecule.

We have also investigated in more detail some selected Cl^-–Bz–$Ar_{(n)}$ systems with $n = 1, 6, 7$ and 15 at several total energies. The case of the Cl^-–$Bz–Ar_1$ aggregate is shown in Fig. 2, where we plot the three components of the configuration energy as a function of the simulation temperature. The Bz–Ar interaction curve (middle panel), with a sigmoidal shape, is indicative of the configuration changes in the Ar solvation shell as the total energy rises and predicts the cluster dissociation for temperatures higher than 130 K. In fact, extra care needs to be taken when simulating Cl^-–$Bz–Ar_1$ clusters at temperature

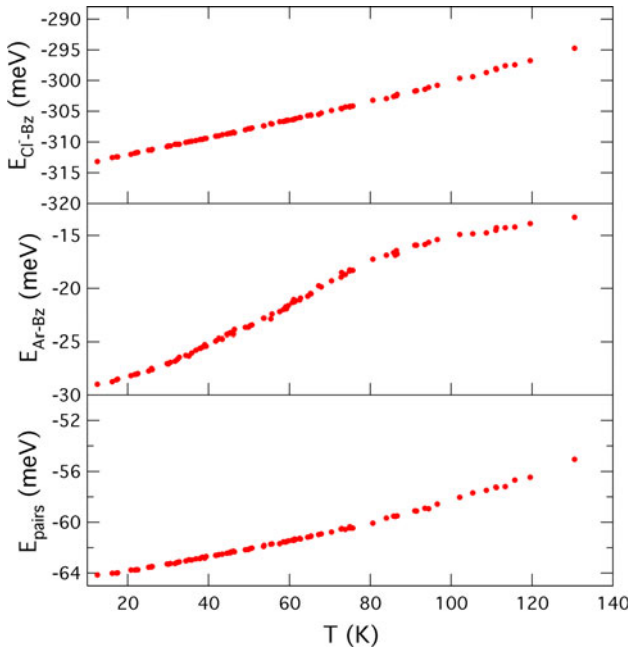

Fig. 2 $E_{Cl^- - Bz}$ (*top panel*), E_{Ar-Bz} (*middle panel*) and E_{pair} (*lower panel*) energy contributions of E_{cfg} for the Cl^-–Bz–Ar_1 aggregate

values higher than 100 K. On the other hand, the chloride–benzene interaction presents a monotonic linear increase with temperature (top panel), revealing that the dimer is simply "pushed apart" by thermal energy. Similar reasoning can be applied to the E_{pairs} component although the slope of the curve is not as constant (lower panel). Our results for this cluster agree with previous calculations for the same cluster [49]. Similar results have been obtained in the case of the Cl^-–Bz–Ar_7 cluster exploring the 20–75 K temperature range, although the trends in the curves are less pronounced. The most significant values are given in Table 5. In order to complete the study, the $n = 6$ and $n = 15$ clusters have been simulated within the 20–35 K range. However, these results do not provide additional information with respect to the $n = 7$ case and are therefore not included in this paper for the sake of briefness.

As it has already been pointed out, this work is focussed also in analyzing geometrical aspects of the Cl^-–Bz dimer solvation. With this purpose in mind, we have obtained the Ar–Bz RDF for all the clusters reported in Table 4 at a temperature of 30 K employing the procedure described in the previous Section. Radial distribution functions have also been computed for Ar atoms with respect to the Cl^- anion. The computed Ar–Bz RDFs are presented in Fig. 3. Let us recall that, as shown in Table 4, all these clusters have available approximately the same kinetic energy (similar T values). Clearly, as more Ar is introduced in the simulation, the solvation shell around the benzene molecule becomes more flexible and Ar atoms explore several potential energy relative minima. The Cl^-–Bz–Ar_1 function presents a single

Table 5 Configuration energy (E_{cfg}) and its components as a function of Temperature (total energy) for the Cl^-–Bz–Ar_7 cluster

T	E_{cfg}	$E_{Cl^- - Bz}$	E_{Ar-Bz}	E_{pairs}
17.1	−989.3	−312.2	−115.9	−561.2
27.0	−976.1	−310.72	−109.2	−556.3
33.5	−965.9	−309.7	−104.78	−551.4
43.5	−948.4	−308.3	−98.7	−541.4
50.8	−936.0	−307.3	−94.4	−534.3
60.1	−921.8	−305.8	−89.6	−526.3
73.0	−903.4	−303.8	−85.1	−514.6

Temperature values are in Kelvin and energies in meV

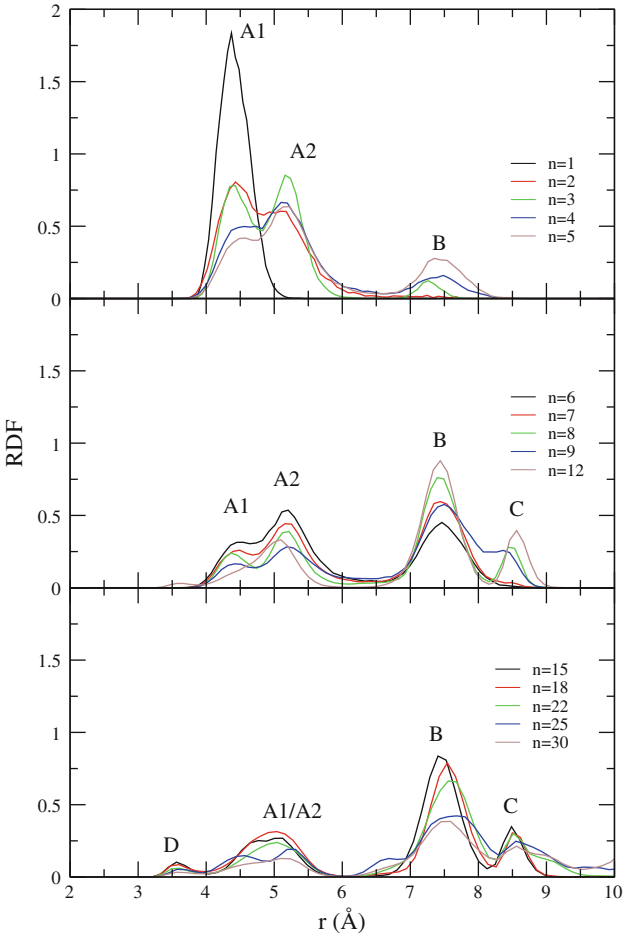

Fig. 3 Ar–Bz RDFs for different Cl^-–Bz–Ar_n aggregates. Evolution with the cluster size (see the text)

maximum (peak A1) for a Bz–Ar distance of approximately 4.5 Å but, as new solvent atoms are added, a new maximum (A2) appears in the RDF at around 5.2 Å, overlapping with the first one. Even for small clusters such as Cl^-–Bz–Ar_3, the presence of a third peak (B) is detected, although very small in intensity, at a distance of 7.5 Å. As the size of the

aggregate increases, this maximum gradually dominates the RDF, becoming the absolute maximum for clusters with $n \geq 7$. The RDF of the cluster with eight Ar atoms reveals the presence of another maximum at an even larger distance, 8.5 Å (peak C), which is conserved as the size of the aggregates increases. Interestingly, the height of peak C remains approximately constant for $8 \leq n \leq 30$. For clusters larger than Cl^-–Bz–Ar_9, peaks A1 and A2 have merged in a broad (relative) maximum (A) and the long distance tail of the RDF increase in intensity. More noticeably, a small maximum at very small distance (3.5 Å, peak D) is detected. The effect of temperature on the Ar–Bz RDF is illustrated in Fig. 4 for the case of the Cl^-–Bz–Ar_7 cluster. As expected, the increase in available energy in the system causes a remarkable broadening of the function, peaks A1 and A2 merge for temperatures above 40 K, and peak B shifts progressively toward slightly larger distance. However, no qualitative changes are observed in the relative height of the three maxima nor in their positions. One can thus conclude that the overall configuration does not change in the 20–70 K temperature range.

On the other hand, the Ar–Cl^- RDF (Fig. 5) is quite plain, presenting a single maximum at 3.7 Å for Cl^-–Bz–Ar_n with $n \leq 9$, revealing the tendency of Ar to solvate preferentially the chloride anion. This claim will be further confirmed by the three-dimensional analysis presented later on. Only when n is greater than 12, additional maxima appear in the RDF. Our full-dimensional treatment of solvation will also illustrate how these maxima are due to the anisotropy caused by the presence of the benzene rather than a second solvation shell around Cl^-. In all the reported simulations, the geometry of the Bz–Cl^- dimer is essentially unaltered by the addition of further Ar solvent atoms and the corresponding RDFs are not shown here. Indeed,

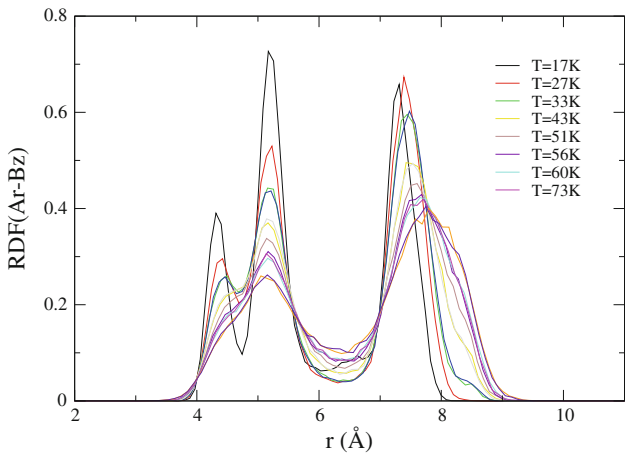

Fig. 4 Ar–Bz RDFs for the Cl^-–Bz–Ar_7 aggregate calculated at several temperatures

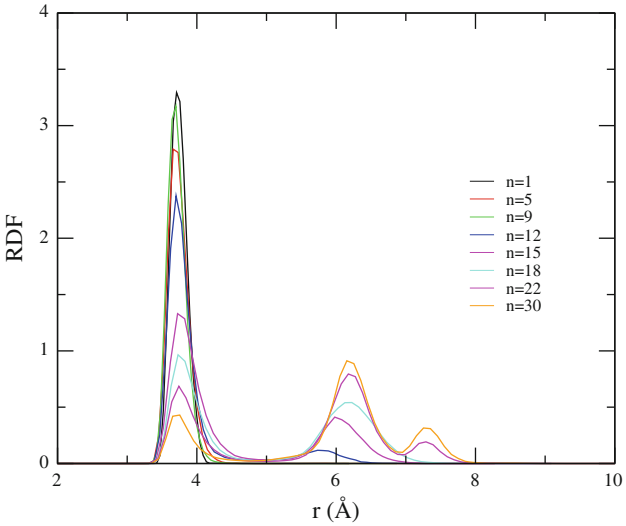

Fig. 5 Ar–Cl^- RDFs for some Cl^-–Bz–Ar_n aggregates at a mean T of 30 K

the maximum of the Bz–Cl^- RDF shifts from 4.84 Å for $n = 2$ to 4.92 Å for $n = 30$. This is not surprising given the much larger interaction energy between the aromatic molecule and the anion with respect to the Ar–Bz one.

Having obtained the Ar–Bz RDF from spherical coordinates of Ar atoms in the mentioned inertial reference frame, we can easily obtain the 2D angular (θ, ϕ) distribution corresponding to the different maxima in the RDF by integrating the probability density between two given values of the radius, r (Eq. 9). This representation provides valuable additional information to the one-dimensional picture given by standard RDFs. Throughout the forthcoming discussion, the reader should keep in mind the spherical coordinate system discussed in Sect. 3. Another important data are the positions of the chloride ion during the MD trajectories. In all our calculations, the halogen anion was located oscillating around $r = 4.9$ Å, $\theta = 90°$ and $\phi = 60°$, this corresponds to a position coplanar to the benzene plane and facing a C–C bond.

We have carried this angular analysis for all the clusters in Table 4, we focus here however on three clusters presenting the most relevant peaks (A1, A2, B, C, D) seen in the RDFs of Fig. 3, namely, $n = 1$, 6 and 12. These are shown in Fig. 6 in different panels corresponding to peak D (bottom right), C (bottom left), B (top right) and the combination of A1 (red contour line) and A2 (blue) (top left). The angular distribution corresponding to peak A1 in Cl^-–Bz–Ar_1 reveals two well-localized peaks at ($\theta = 140°$, $\phi = 60°$) and ($\theta = 40°$, $\phi = 60°$). These maxima are symmetric and reveal that the most visited geometries during the MD trajectory corresponds to an Ar out of the Bz–Cl^- plane by 40°, either above or below, and aligned with the Bz c.o.m. and the Cl^- anion ($\phi = 60°$). Almost the

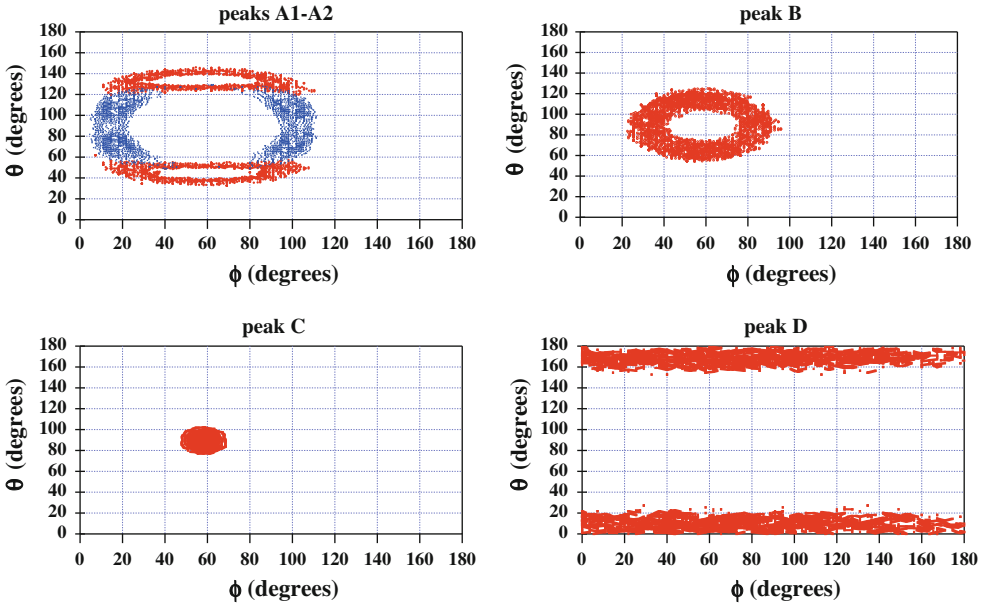

Fig. 6 Angular distribution analysis of the most relevant peaks of the Ar–Bz RDFs of Fig. 3 for the Cl^-–Bz–Ar_6 and Cl^-–Bz–Ar_{12} aggregates (see the text for details)

same angular distribution is obtained for the same peak in the case of the Cl^-–Bz–Ar_6 cluster. The only difference is that the distribution is broader in the azimuthal angle (ϕ), probably distorted by the overlap with peak A2. The A2 peak in the same cluster, instead, has an angular distribution quite spread in the θ coordinate between 50° and 130° interval, with two maxima at 65° and 115° but sharply centered around 17° and 100° in the ϕ coordinate. The combination of the angular distribution of these two peaks (top left panel) nicely corresponds to an arrangement in which the 6 Ar atoms form a hexagon perpendicular to the Bz plane and maximizing the interaction with both the Bz and the Cl^-. The following RDF maximum studied has been peak B (7.5 Å) present in all clusters with $n \geq 5$. The angular distribution analysis in both Cl^-–Bz–Ar_6 and Cl^-–Bz–Ar_{12} clusters are identical and therefore only the $n = 6$ one is shown in the top right panel of Fig. 6. The probability density is concentrated in a circular band and corresponds to a second arrangement of Ar atoms parallel to the first one (peak A1/A2) and farther away from the Bz c.o.m. Finally, the additional peaks C and D appearing the RDFs of the larger clusters have a clearly different pattern concerning their angular distributions. Their corresponding angular distributions have been analyzed using the Cl^-–Bz–Ar_{12} probability density. Peak C (Fig. 6, left bottom panel) presents a single maximum at precisely the same angular coordinates as the chloride anion and corresponds to an Ar atom located right behind the Cl^- atom (Cl^- is at 4.9 Å from the Bz c.o.m., and the peak is located at 8.5 Å). On the other hand, the angular distribution for peak D (Fig. 6, right bottom panel) is strongly localized at $\theta = 0°$ or $\theta = 180°$ and completely delocalized in ϕ. This makes sense since the Ar atom is the right on top (or below) of the benzene molecule and the azimuthal angle cannot be properly defined. In all cases, however, it is interesting to note that all the reported angular distributions are symmetric with respect to the Cl^- coordinates ($\theta = 90°$, $\phi = 60°$), indicating that the main driving force is the solvation of the halogen anion.

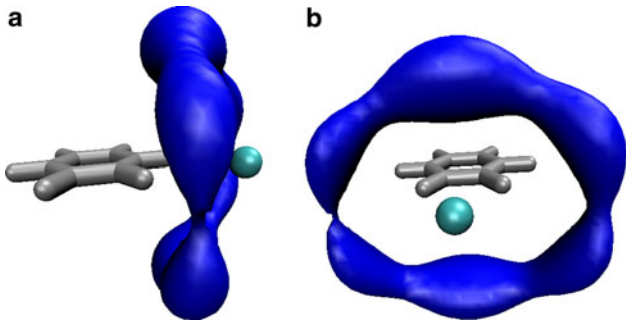

Fig. 7 Mass weighted probability density isosurface (1.06) plot of the Ar probability density in the Cl^-–Bz–Ar_6 cluster

Our angular distribution analysis is finally confirmed by visualizing the 3D probability density, introducing our simulation data (properly shifted to the inertial reference frame) into the VMD visualization program. The Volmap tool included in the mentioned package has allowed us to visualize isosurface of (mass weighted) constant probability density for the Ar atoms in our simulations. These isosurfaces can be interpreted as "*argon orbitals*". As the most representative cases, Figs. 7, 8, 9 contain probability density isosurfaces for the Cl^-–Bz–Ar_6 and Cl^-–Bz–Ar_{12} clusters. First, Fig. 7 shows the isosurface with higher probability density value in the $n = 6$ cluster. This probability band perfectly matches our reasoning for the A1 and A2 overlapping peaks in the RDF, and solvent atoms are

arranged in a hexagon between the aromatic molecule and the halogen anion. The shape of the isosurface nicely correlates with the angular distribution of Fig. 6 (top left panel). In the case of the Cl^-–Bz–Ar_{12}, we present isosurfaces for two different values of the probability density. Figure 8 corresponds to a large value of the probability density in which we can identify the arrangements corresponding to peaks A1-A2, B and C. The description given in the paragraph above in terms of angular distribution fully matches the orbital visualization. Peak A1/A2 can immediately be associated with the ring at a shorter distance to the Bz c.o.m. The next ring is identified with peak B, while peak C, with the same spherical coordinates as the Cl^- but a larger radius, corresponds to the lobe placed right behind the anion. In order to visualize the probability density that gives rise to peak D in the RDF, we need to plot an isosurface for a low density value (the peak is very small). Indeed, the 0.21 isosurface shown in Fig. 9 presents two lobes, one on top of the c.o.m. of benzene and another on right below, both along the Bz C_6 symmetry axis, matching the angular distribution obtained for peak D. These features reported for the n = 1, 6 and 12 cluster do not correspond to some magical number and have been observed in all the clusters studied. No new structure can be seen when we represent for instance the Cl^-–Bz–Ar_{30} probability density, only more solvent atoms are added to the band corresponding to peak D and its angular representation becomes less centered at theta = 0. We interpret this as the formation of a third ring, which we do not believe will be six membered.

The use of spherical coordinates in an inertial reference offers the additional possibility of exploring cluster isomerization following not only radial changes along the dynamics but also changes in the angular position. This will be the subject of future thorough studies but we would like however to include in this work two figures which illustrate, first, the active dynamics of solvation and, secondly, the different isomerization processes. Figure 10 presents the spherical coordinates of a chosen Ar atom along the MD trajectory of a Cl^-–Bz–Ar_5 cluster at 30 K. The solvent atom "jumps" between $r \sim 5$ Å and $r \sim 7.5$ Å, the two main peaks in the corresponding RDF. However, the time spent at the longer distance is significantly shorter, of the order of 200 ps.A similar behavior cannot be observed along the θ and ϕ coordinates where the changes

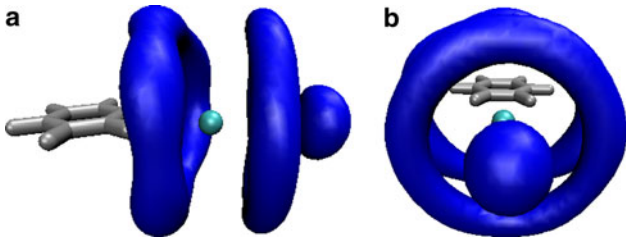

Fig. 8 Isosurface (1.25) plot of the Ar probability density in the Cl^-–Bz–Ar_{12} cluster

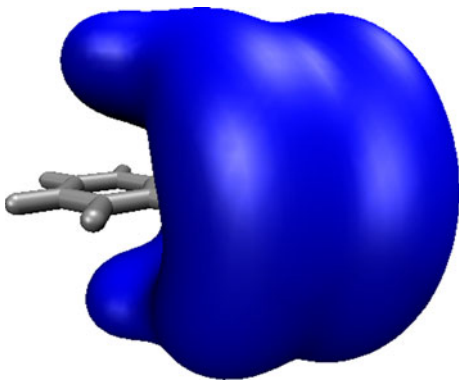

Fig. 9 Isosurface (0.21) plot of the Ar probability density in the Cl^-–Bz–Ar_{12} cluster

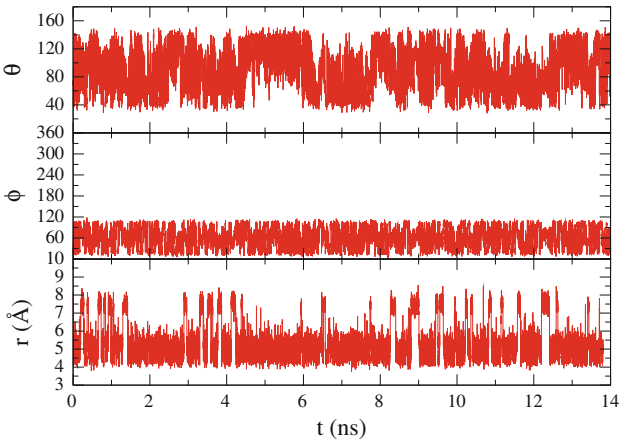

Fig. 10 Cl^-–Bz–Ar_5 aggregate: Trajectory of a selected Ar atom in spherical coordinates (see text)

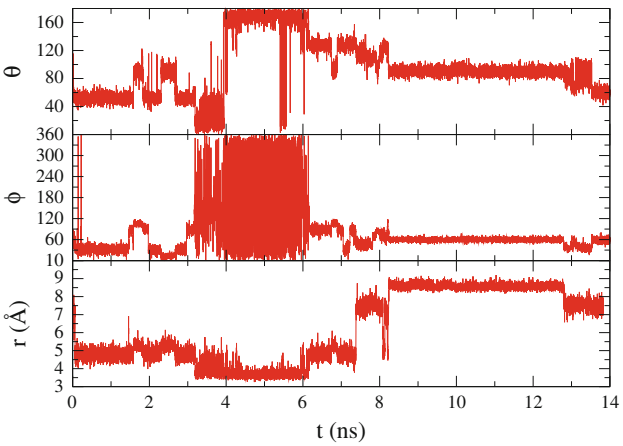

Fig. 11 Cl^-–Bz–Ar_{15} aggregate: Trajectory of a selected Ar atom in spherical coordinates (see text)

are too fast. The situation is qualitatively different in the Cl^-–Bz–Ar_{15} cluster (Fig. 11). First, oscillations are not as broad as in the $n = 6$ case, probably an indication that the solvation shell is more complete and the cluster more stable. Secondly, isomerizations can be clearly identified in all three coordinates and the lifetimes increase considerably. As already mentioned, the detailed study of cluster isomerization using these coordinates will be subject of investigation in the future.

5 Concluding remarks

The dynamics of different Cl^-–Bz–Ar_n aggregates have been investigated from molecular dynamics simulations. An analytical potential energy function constructed by means of two-body, three-body (atom(ion)-bond) and electrostatic interactions has been employed for this purpose. Two-body and three-body nonelectrostatic contributions have been represented by means of the ILJ function, while the electrostatic one has been calculated using the Coulomb law, which has been applied between the negative charge of Cl^- and punctual charges placed on Bz molecule, which preserve the asymptotic behavior of the ion-quadrupole interaction. Solvation effects on Cl^-–Bz clusters have been investigated by employing Ar atoms as a solvent. A maximum of 30 solvent atoms have been included in our molecular dynamics simulations. The microscopic solvation phenomena, clearly manifested by the existence of several microenvironments corresponding to different minima in the potential energy surface, have been investigated. To better understand these phenomena, RDFs, angular distributions, as well as 3D analysis of the Ar, and probability density have been extracted from our MD simulation. The preference of Ar atoms to be placed maximizing the Ar–Cl interaction but in such a way to interact with both Bz and Cl^- has been observed by increasing the number of solvent atoms. The evolution of the different energy components has been analyzed for the Cl^-–Bz–Ar cluster with increasing total energy and cluster size. The presented scheme, employing an inertial reference frame centered on the Bz molecule and relative spherical coordinates of the Ar atoms, provides a greater insight into the dynamics of solvation, going beyond the standard one-dimensional radial distribution functions. Our angular distributions calculated for each maximum of the Ar–Bz RDF have revealed the three-dimensional ordering of the Ar solvation shell. The visualization of probability density isosurfaces has confirmed our observations.

Acknowledgments The authors acknowledge financial support from the Ministerio de Educación y Ciencia (Spain, Projects CTQ2009-12215 and CTQ2007-61109) and the Generalitat de Catalunya (Project 2009-SGR 17). Also thanks are due to the Centre de Supercomputació de Catalunya CESCA-C4 and Fundació Catalana per a la Recerca for the allocated supercomputing time. M. Albertí acknowledges financial support from the Ministerio de Ciencia e Innovación (Spain, Mobility Program, Project PR2008-0251).

References

1. Alonso JL, Antolínez S, Bianco S, Lesarri A, López JC, Caminati W (2004) J Am Chem Soc 126:3244
2. Cabarcos OM, Weinheimer CJ, Lisy JM (1998) J Chem Phys 108:5151
3. Kumpf RA, Dougherty DA (1993) Science 271:163
4. Dougherty DA (1996) Science 261:1708
5. Ma JC, Dougherty DA (1997) Chem Rev 97:1303
6. Cabarcos OM, Weinheimer CJ, Lisy JM (1999) J Chem Phys 110:8429
7. Morais-Cabral JH, Zhou Y, MacKinnon R (2001) Nature 414:37
8. Mecozzi S, West AP Jr, Dougherty DA (1966) Proc Natl Acad Sci 93:10566
9. Tsuzuki S, Yoshida M, Uchimaru T, Mikami M (2001) J Phys Chem A 105:769
10. Felder C, Jiang HL, Zhu WL, Chen KX, Silman I, Botti SA, Sussman JL (2001) J Phys Chem A 105:1326
11. Mecozzi S, West AP, Dougherty DA (1996) J Am Chem Soc 118:2307
12. Cubero E, Luque FJ, Orozco M (1998) Proc Natl Acad Sci USA 95:5976
13. Caldwell JW, Kollman PA (1995) J Am Chem Soc 117:4177
14. Nicholas JB, Hay BP, Dixon DA (1999) J Phys Chem A 103:1394
15. Quiñonero D, Garau C, Frontera A, Ballester P, Costa A, Deyà PM (2005) J Phys Chem A 109:4632
16. Jalbout AF, Adamowicz L (2002) J Chem Phys 116:9672
17. Luhmer M, Bartik K, Dejaegere A, Bovy P, Reisse J (1994) Bull Soc Chim Fr 131:603
18. Williams JH (1993) Acc Chem Res 26:593
19. Kim D, Lee ECX, Kim KS, Tarakeshwar P (2007) J Phys Chem A 111:7980
20. Bianchi A, Bowman-James K, García-España E (eds) (1997) Supramolecular chemistry of anions. Wiley, New York
21. Imai YN, Inoue Y, Nakanishi I, Kitaura K (2008) Protein Sci 17:1129
22. Li Y, Flood AH (2008) J Am Chem Soc 130:12111
23. Alcalde E, Mesquida N, Vilaseca M, Alvarez-Rúa C, García-Granda S (2007) Supramol Chem 19:501
24. Cerichelli G, Mancini G (2000) Langmuir 16:182
25. Mascal M, Armstrong A, Bartberger MD (2002) J Am Chem Soc 124:6274
26. Schneider H, Vogelhuber KM, Shinle F, Weber JM (2007) J Am Chem Soc 129:13022
27. Garau C, Frontera A, Quiñonero D, Ballester P, Costa, A, Deyà PM (2003) Chem Phys Chem 4:1344
28. Garau C, Quiñonero D, Frontera A, Costa A, Ballester P, Deyà PM (2003) Chem Phys Lett 370:7
29. Beer PD, Galle PA (2001) Angw Chem Int Ed 40:486
30. Schottel BL, Chifotides HT, Dunbar KR (2008) Chem Soc Rev 37:68
31. Douin S, Parneix P, Amar FG, Bréchignac P (1997) J Phys Chem A 101:122
32. Amirav A, Even U, Jortner J (1981) J Chem Phys 75:2489
33. Leutwyler S, Jortner J (1987) J Phys Chem 91:5558
34. Leutwyler S, Bösiger J (1990) Chem Rev 90:489
35. Pirani P, Brizi S, Roncaratti LF, Casavecchia P, Cappelletti D, Vecchiocattivi F (2008) Pys Chem Chem Phys 10:5489

36. Faginas Lago N, Huarte Larrañaga F, Albertí M (2009) Eur Pys J D 55:75
37. Pirani F, Albertí M, Castro A, Moix M, Cappelletti D (2004) Chem Phys Lett 394:37
38. Albertí M, Castro A, Laganà A, Pirani F, Porrini M, Cappelletti D (2004) Chem Phys Lett 392:514
39. Albertí M (2010) J Phys Chem A 114:2266
40. Albertí M, Aguilar A, Lucas JM, Pirani F, Cappelletti D, Coletti C, Re N (2006) J Phys Chem A 110:9002
41. Albertí M, Aguilar A, Lucas JM, Pirani F, Coletti C, Re N (2009) J Phys Chem A 113:14606
42. Coletti C, Re N (2006) J Phys Chem A 110:6563
43. Coletti C, Re N (2009) J Phys Chem A 113:1578
44. Albertí M, Aguilar A, Lucas JM, Laganà A, Pirani F (2007) J Phys Chem A 111:1780
45. Albertí M, Castro A, Laganà A, Moix M, Pirani F, Cappelletti D, Liuti G (2005) J Phys Chem A 109:2906
46. Albertí M, Aguilar A, Lucas JM, Cappelletti D, Laganà A, Pirani F (2006) Chem Phys 328:221
47. Huarte-Larrañaga F, Aguilar A, Lucas JM, Albertí M (2007) J Phys Chem A 111:8072
48. Albertí M, Aguilar A, Lucas JM, Pirani F (2009) Theor Chem Acc 123:21
49. Albertí M, Castro A, Laganà A, Moix M, Pirani F, Cappelletti D (2006) Eur Pys J D 38:185
50. Maitland GC, Rigby M, Smith EB, Wakeham WA (1987) Intermolecular forces. Oxford University Press, New York
51. Sunner J, Nishizawa K, Kebarle P (1981) J Phys Chem 85:1814
52. Pirani F, Cappelletti D, Liuti G (2001) Chem Phys Lett 350:286
53. http://www.dl.ac.uk/TCSC/Software/DL_POLY
54. Humphrey W, Dalke A, Schulten K (1996) VMD–Visual molecular dynamics. J Molec Graphics 14:33